

## Pressure statistics of gas nuclei in homogeneous isotropic turbulence with an application to cavitation inception

Cite as: Phys. Fluids **32**, 095107 (2020); <https://doi.org/10.1063/5.0019683>

Submitted: 24 June 2020 . Accepted: 12 August 2020 . Published Online: 03 September 2020

 Mehedi H. Bappy,  Pablo M. Carrica,  Alberto Vela-Martín,  Livia S. Freire, and  Gustavo C. Buscaglia

### COLLECTIONS

 This paper was selected as an Editor's Pick



[View Online](#)



[Export Citation](#)



[CrossMark](#)

### ARTICLES YOU MAY BE INTERESTED IN

[A numerical study of particle jetting in a dense particle bed driven by an air-blast](#)  
Physics of Fluids **32**, 093301 (2020); <https://doi.org/10.1063/5.0015190>

[Visualizing droplet dispersal for face shields and masks with exhalation valves](#)  
Physics of Fluids **32**, 091701 (2020); <https://doi.org/10.1063/5.0022968>

[Sound propagation in porous materials containing rough tubes](#)  
Physics of Fluids **32**, 093604 (2020); <https://doi.org/10.1063/5.0017710>

**Physics of Fluids**  
**SPECIAL TOPIC:** Tribute to  
Frank M. White on his 88th Anniversary

**SUBMIT TODAY!**

# Pressure statistics of gas nuclei in homogeneous isotropic turbulence with an application to cavitation inception



Cite as: Phys. Fluids 32, 095107 (2020); doi: 10.1063/5.0019683

Submitted: 24 June 2020 • Accepted: 12 August 2020 •

Published Online: 3 September 2020



Mehedi H. Bappy,<sup>1</sup> Pablo M. Carrica,<sup>1,a)</sup> Alberto Vela-Martín,<sup>2</sup> Livia S. Freire,<sup>3</sup> and Gustavo C. Buscaglia<sup>3</sup>

## AFFILIATIONS

<sup>1</sup>IHR-Hydroscience and Engineering, University of Iowa, Iowa City, Iowa 52242, USA

<sup>2</sup>ETSIAE, Universidad Politécnica de Madrid, Madrid 28040, Spain

<sup>3</sup>Instituto de Ciências Matemáticas e de Computação, Universidade de São Paulo, São Carlos, Brazil

<sup>a)</sup>Author to whom correspondence should be addressed: pablo-carrica@uiowa.edu

## ABSTRACT

The behavior of the pressure along the trajectories of finite-sized nuclei in isotropic homogeneous turbulence is investigated using direct numerical simulations at  $Re_\lambda = 150$ . The trajectories of nuclei of different sizes are computed by solving a modified Maxey–Riley equation under different buoyancy conditions. Results show that larger nuclei are more attracted to the vortex cores and spend more time at low-pressure regions than smaller nuclei. The average frequency of pressure fluctuations toward negative values also increases with size. These effects level off as the Stokes number becomes greater than 1. Buoyancy, characterized by the terminal velocity  $w$ , counteracts the attraction force toward vortex cores while simultaneously imposing an average vertical drift between the nuclei and the fluid. Computational results indicate that weak vortices, associated with moderately low pressures, lose their ability to capture finite-sized nuclei if  $w \geq u'$ . The attraction exerted by the strongest vortices on the largest of the considered nuclei, on the other hand, can only be overcome by buoyancy if  $w \geq 8u'$ . The quantitative results of this study are shown to have a significant impact on modeling cavitation inception in water. For this purpose, the Rayleigh–Plesset equation is solved along the nuclei trajectories with realistic sizes and turbulence intensities. The simulations predict cavitation inception at mean pressures several kPa above vapor pressure.

Published under license by AIP Publishing. <https://doi.org/10.1063/5.0019683>

## I. INTRODUCTION

Many environmental and industrial processes deal with the transport of particles suspended in different carrier fluids. Some examples are sediment transport, plankton-algae dynamics, combustion mixing, pollutant dispersion, cloud-rain formation, and bubbly flow in chemical reactors, among many others. These particles, which could be solid, liquid (droplets), or gaseous (bubbles), travel within the flow and are subject to the local flow variables (e.g., pressure, temperature, and humidity). The study discussed here focuses on the pressure fluctuations experienced by the suspended particles in turbulent flow. It is motivated by the presence of gas nuclei in the liquid flow around general lifting surfaces and propellers or in turbines, pumps, spillways, control valves, and engines.

Depending on the pressure history experienced by each nucleus, the phenomenon known as cavitation can take place, which is particularly critical due to its adverse effects of vibration, noise, and erosion.<sup>1,2</sup>

As the working conditions of a hydraulic device are varied and its minimum pressure is decreased, the first instances of cavitation in the flow are known as *cavitation inception*. The ability to predict cavitation inception is important to understand its causes and improve the device's design. If the flow is turbulent, the statistics of the random pressure fluctuations *along the particles' paths* (i.e., *Lagrangian* statistics) have an impact on the initial presence of cavitation.<sup>3</sup> Quantifying this impact in technologically relevant flows is thus an essential ingredient for predictive models of cavitation inception. Recently, Agarwal *et al.*<sup>4</sup> presented experimental evidence

relating pressure fluctuation statistics to cavitation inception for a backward facing step flow. While complex turbulent flows often result in canonical vortex interaction leading to cavitation inception (see, for instance, Refs. 5 and 6), homogeneous isotropic turbulence provides a flow that approximates the sub-grid models for large eddy simulation (LES) and is thus of academic and practical interest.<sup>7</sup>

Pressure fluctuations in homogeneous isotropic turbulence have been extensively studied theoretically, experimentally, and numerically. Batchelor<sup>8</sup> studied different spatial correlations involving pressure fluctuations in homogeneous turbulence. He found the root mean square of pressure fluctuations to be  $0.58\sqrt{\langle u'^2 \rangle}$  (where  $u'$  is the turbulence intensity) and determined a correlation to estimate the pressure gradient in the flow based on the diffusion rate of marked particles from a fixed source.

These analyses were further developed by Uberoi.<sup>9</sup> The advent of Direct Numerical Simulation (DNS) allowed for more detailed investigations. Pumir<sup>10</sup> numerically studied pressure fluctuations in three-dimensional homogeneous isotropic turbulence for a range of Reynolds numbers ( $Re_\lambda = 21.6\text{--}77.5$ , where  $Re_\lambda = \lambda u' / \nu$ ). He reported that the probability density function (pdf) of the pressure has an exponential tail on the negative side for  $Re_\lambda < 60$ , becoming super exponential for larger  $Re_\lambda$ . Holzer and Siggia<sup>11</sup> analytically confirmed that at very low pressure, the pressure probability density function of a Gaussian velocity field has negative skewness and exponential tail. Cao *et al.*<sup>12</sup> used conditional averaging in high-resolution DNS to investigate statistical relations among pressure, vorticity, dissipation, and kinetic energy. According to their study, the negative tail becomes super-exponential and moves upward as  $Re_\lambda$  increases. A strong correlation of high vorticity with low pressure was reported by Cao *et al.*<sup>12</sup> and Pumir<sup>10</sup> through qualitative analysis of pressure–vorticity iso-surface visualization.

The Lagrangian statistics of pressure, with focus on their time dependence, were first computed in a recent work by Bappy *et al.*<sup>13</sup> They considered neutral tracer particles and extracted the frequency and duration of Lagrangian low-pressure events from DNS data. However, depending on density and size, particle motion may be quite different from that of a tracer. Studies have shown that lighter particles preferentially concentrate in high-vorticity regions and heavy particles concentrate in high-strain regions and that this effect increases with particle size.<sup>14</sup> The statistics of Lagrangian pressure fluctuations thus depend on the size of the particle, increasing the probability of lower pressures for gaseous nuclei as their size increases.

This is one of the mechanisms by which cavitation inception and cavitation dynamics depend on the nuclei size distribution.<sup>15–19</sup> Recently, Bappy *et al.*<sup>20</sup> reported some preliminary results showing that nuclei size has a very significant impact on Lagrangian pressure statistics: larger nuclei are more attracted to the low-pressure vortex cores and stay there longer, experiencing more and longer low pressure events.<sup>20</sup> This article significantly extends those results in three ways. First, the statistical significance of the results is improved by a fourfold increase in the simulated time, allowing for a more meaningful and detailed analysis. Second, buoyancy effects are incorporated into the study. Mathai *et al.*<sup>21</sup> did an excellent review on bubbles and buoyant particles in turbulence and discussed their importance in contrast to neutrally buoyant and heavy particles. Ruetsch and Meiburg<sup>22</sup> showed, with an example of bubbles around

a Stuart vortex, that buoyancy can have a significant impact on the entrapment of bubbles inside vortices. Third, the direct consequences of the Lagrangian pressure fluctuations on cavitation prediction are demonstrated with a concrete example. The Rayleigh–Plesset equation that models bubble expansion is solved with the nuclei pressure histories as forcing, computing the frequency of explosive growth events and thus the efficiency of low-pressure fluctuations to produce cavitation of the nuclei.

## II. METHODS

### A. Turbulence dataset

The DNS database of homogeneous isotropic turbulence is obtained by solving the incompressible Navier–Stokes (NS) equations,

$$\partial_t u_i + u_j \partial_j u_i = -\partial_i p + \nu \partial_{kk} u_i + f_i, \quad (1)$$

$$\partial_i u_i = 0, \quad (2)$$

in a three-dimensional, periodic domain on the basis of  $N/2$  Fourier modes in each direction. In (1) and (2),  $u_i$  is the  $i$ th component of the velocity vector,  $p$  is the modified pressure,  $\nu$  is the kinematic viscosity, and  $f_i$  is a body-force term per unit mass. The repeated indices imply summation.

The non-linear terms of the NS equations are fully dealiased by the phase-shifting procedure. A third-order Runge–Kutta method with semi-implicit treatment of the linear terms is used for the time integration. To sustain turbulence in a steady state, a linear body-force is implemented,  $\hat{f}_i = \gamma \hat{u}_i$ , which is only applied to low wavenumbers ( $|\mathbf{k}| < 2$ ), where  $\hat{\cdot}$  denotes the Fourier transform and  $\mathbf{k}$  is the wavenumber vector. The forcing coefficient is set so that, at each time, the total kinetic energy injected in the system is constant and equal to the time- and volume-averaged dissipation,  $\epsilon$ , i.e.,

$$\gamma = \frac{\epsilon}{\sum_{|\mathbf{k}| \geq 2} \hat{u}_i(\mathbf{k}, t) \hat{u}_i^*(\mathbf{k}, t)} : |\mathbf{k}| < 2, \quad (3)$$

$$\gamma = 0 : |\mathbf{k}| \geq 2. \quad (4)$$

In Eq. (3),  $(\cdot)^*$  denotes the complex conjugate and the sum in the denominator is the kinetic energy contained above  $|\mathbf{k}| = 2$  at each time. The dissipation  $\epsilon$  is set equal to unity and the kinematic viscosity  $\nu$  is tuned to keep a numerical resolution  $r = k_{\max} \eta = 1.5$ , where  $\eta = (\nu/\epsilon^4)^{3/4}$  is the Kolmogorov length scale and  $k_{\max} = \sqrt{2N}/3$  is the maximum wavenumber magnitude. For a fixed resolution, the kinematic viscosity is  $\nu = (r/k_{\max})^{4/3}$ . The time scales associated with the Kolmogorov and integral length scales are  $t_\eta = (\eta^2/\epsilon)^{1/3}$  and  $t_L = L/u'$ , respectively, with  $u'$  being the amplitude of the velocity fluctuations and  $L = \int_0^\infty \frac{E(k)}{k} dk / \int_0^\infty E(k) dk$  being the integral length scale. The Taylor microscale Reynolds number is  $Re_\lambda = \lambda u' / \nu$ , where  $\lambda = u' \sqrt{15(\nu/\epsilon)}$  is the Taylor microscale.

For the adimensionalization of the equations, the Taylor microscale  $\lambda$ , the velocity fluctuation intensity  $u'$ , and the liquid density  $\rho$  are used as reference length, velocity, and density, respectively. The nondimensional coordinates, velocities, accelerations, pressure,

time, and particle radius are computed, respectively, as

$$\tilde{\mathbf{x}} = \mathbf{x}/\lambda, \quad (5)$$

$$\tilde{\mathbf{u}} = \mathbf{u}/u', \quad (6)$$

$$\tilde{\mathbf{a}} = \mathbf{a}\lambda/u'^2, \quad (7)$$

$$\tilde{p} = p/(\rho u'^2), \quad (8)$$

$$\tilde{t} = tu'/\lambda, \quad (9)$$

$$\tilde{R} = R/\lambda. \quad (10)$$

Note that the choice of the Taylor microscale as reference length scale is arbitrary and the Kolmogorov length scale could have been chosen instead, leading to the use of the Kolmogorov time scale  $t_\eta = \sqrt{v/\epsilon}$  as a reference time scale instead of  $\lambda/u'$ .

In Secs. II B–III D, all the variables presented are in nondimensional form, omitting the tilde ( $\tilde{\cdot}$ ) to ease the notation. Dimensional variables (and the tilde notation for nondimensional ones) are used again in Sec. IV.

## B. Model of bubble motion

For the computation of trajectories (i.e., tracking), the nuclei are modeled as small, spherical, and non-interacting particles moving in the turbulence fields with fixed radius  $R_0$ . The Stokes law gives its non-dimensional inertial time  $\tau$  as

$$\tau = \frac{Re_\lambda}{9} R_0^2. \quad (11)$$

The Stokes number  $St = \tau/t_\eta$  is then related to  $R_0$  by em  $St = 64.6R_0^2$  when  $Re_\lambda = 150$ .

The trajectories of the nuclei in the turbulence field are computed by integrating

$$\frac{d\mathbf{x}(t)}{dt} = \mathbf{v}(t), \quad (12)$$

where  $\mathbf{x}(t)$  and  $\mathbf{v}(t)$  are the nucleus' position and velocity at time  $t$ , respectively, and  $d/dt$  represents the time derivative along the particle trajectory. The initial condition is  $\mathbf{x}(0) = \mathbf{x}_0$ .

The velocity  $\mathbf{v}$  of a finite-sized particle differs from that of the fluid surrounding it. If the particle diameter is small compared to the Kolmogorov length scale  $\eta$ , a simple equation can be written for  $\mathbf{v}$ , namely,

$$\frac{d\mathbf{v}}{dt} = \frac{1}{\tau}(\mathbf{u} + \mathbf{w} - \mathbf{v}) + 2\mathbf{a} + \frac{d\mathbf{u}}{dt}. \quad (13)$$

In the above equation,  $\mathbf{u}$  and  $\mathbf{a}$  are the fluid velocity and acceleration at the particle position and at time  $t$ , respectively, and  $\mathbf{w}$  is the non-dimensional bubble terminal velocity, which is taken as  $\mathbf{w} = w\hat{\mathbf{e}}$ , where  $\hat{\mathbf{e}}$  is the vertical unit vector and  $w$  is a parameter that depends on the bubble size, which will be referred to as a *buoyancy parameter*. For Stokes flow, the dimensionless terminal velocity is  $w = \frac{2}{9}gR_0^2Re_\lambda$ . We assumed that  $w$  is an independent parameter because  $g$  is, in principle, an independent parameter (one could be studying cavitation on Mars or in an accelerating rocket). In normal conditions, in

the Earth,  $g$  is fixed and  $w$  is dependent only on turbulence parameters (that determine the dimensionless  $g$  and  $Re_\lambda$ ) and  $R_0$ ; thus,  $R_0$  is the only parameter other than the quantities defining the turbulence. In this case, the dimensionless terminal velocity can be rewritten as  $w = \frac{2}{9}R_0^2 \times \frac{9.81}{u'^2}$ . An upper limit for  $w$  can be determined by using the largest nuclei radius  $R_0$  and the smallest  $u'$  of interest. For typically large nuclei  $R_0 = 100 \mu\text{m}$ , we have  $w = \frac{0.0218}{u'}$ .

Equation (14) is solved with the initial condition  $\mathbf{v}(0) = \mathbf{v}_0$ , which in all computations is set equal to the local fluid velocity  $\mathbf{u}(\mathbf{x}_0, 0)$ . Maxey and Riley<sup>23</sup> used this equation to model the motion of small particles in an unsteady Stokes flow. Several authors<sup>22,24,25</sup> later proposed a corrected form of (13) by replacing the added mass term  $d\mathbf{u}/dt$  by the fluid acceleration  $\mathbf{a}$ . The corrected equation reads

$$\frac{d\mathbf{v}}{dt} = \frac{1}{\tau}(\mathbf{u} + \mathbf{w} - \mathbf{v}) + 3\mathbf{a}. \quad (14)$$

For a low Reynolds number, the instantaneous difference between the two approaches is small,<sup>23</sup> yet upon integration, this difference can cause a noteworthy change in the particle trajectory and pressure history.<sup>20</sup> All the results presented in this article are obtained using (14), which is the nowadays favored form of the model. Equation (14) incorporates the effects of Stokes drag, buoyancy, added mass, and fluid acceleration, while the Basset–Boussinesq history and the Faxén correction terms are neglected.

The main outcome of the tracking computations, for each  $R_0$ , is a set of particle trajectories  $\{\mathbf{x}^{(i)}(t)\}$  ( $i = 1, \dots, M$ , with  $M$  being the number of particles), obtained by solving (12) and (14) from  $t = 0$  to  $t = T$  with different initial positions  $\{\mathbf{x}_0^{(i)}\}$ . Along each of these trajectories, the local pressure field is stored as the *pressure history*  $P^{(i)}$  of the particle. For the  $i$ th particle, the definition reads

$$P^{(i)}(t) = p(\mathbf{x}^{(i)}(t), t). \quad (15)$$

In Sec. III, the impact of size ( $R_0$ ) and of buoyancy (quantified by  $w$ ) on the pressure statistics of the suspended gas nuclei in the DNS flow are evaluated.

## C. Numerical algorithm for tracking

An unconditionally stable, second-order semi-implicit predictor–corrector scheme<sup>20</sup> has been used for numerical integration of the coupled equations (12) and (14). For  $n = 0, 1, 2, \dots$ , considering the variables at time  $t_n$  already computed, the algorithm proceeds as follows:

### 1. Predictor

$$\mathbf{x}^* = \mathbf{x}^n + \Delta t \mathbf{v}^n, \quad (16)$$

$$\mathbf{u}^* = \mathbf{u}(\mathbf{x}^*, t^{n+1}), \quad (17)$$

$$\mathbf{v}^* = \frac{\mathbf{v}^n + \Delta t \left[ \frac{\mathbf{u}^* + \mathbf{w}}{\tau} + 3\mathbf{a}^n \right]}{1 + \frac{\Delta t}{\tau}}. \quad (18)$$

### 2. Corrector

$$\mathbf{x}^{n+1} = \mathbf{x}^n + \frac{\Delta t}{2} (\mathbf{v}^n + \mathbf{v}^*), \quad (19)$$

$$\mathbf{u}^{n+1} = \mathbf{u}(\mathbf{x}^{n+1}, t^{n+1}), \quad (20)$$

$$\mathbf{a}^{n+1} = \mathbf{a}(\mathbf{x}^{n+1}, t^{n+1}), \quad (21)$$

$$\mathbf{v}^{n+1} = \frac{1}{(1 + \frac{\Delta t}{2\tau})} \left[ \mathbf{v}^n + \frac{\Delta t}{2} \left( 3(\mathbf{a}^n + \mathbf{a}^{n+1}) + \frac{\mathbf{u}^n + \mathbf{u}^{n+1} + 2\mathbf{w} - \mathbf{v}^n}{\tau} \right) \right]. \quad (22)$$

Equations (17), (20), and (21) represent spatial interpolations, at time  $t^{n+1}$ , of the DNS fields  $\mathbf{u}$  and  $\mathbf{a}$ . A three-dimensional third-order polynomial scheme is adopted for this operation.

The DNS is solved with very high temporal resolution (time step equal to  $t_\eta/240$ ). Since it is very costly to track and store the variables of all the particles, we adopted a coarser time step to integrate the trajectories. Equations (16)–(22) are solved at every fourth DNS time step with corresponding  $\Delta t = 4.3 \times 10^{-3}$ . This makes  $\Delta t$  60 times smaller than Kolmogorov timescale ( $\Delta t \approx t_\eta/60$ ), providing a good compromise between accuracy and computational cost. A time step study was performed to check that pressure statistics do not change upon further reduction in  $\Delta t$ .

#### D. Low-pressure events

A set of negative pressure thresholds is defined as  $p_- = -2.0, -2.2, -2.4, \dots$  to represent various levels of low-pressure fluctuations experienced by the Lagrangian particles. If a nucleus experiences a pressure history  $P(t)$ , we define a low-pressure event with threshold  $p_-$  and starting time  $t_{\text{start}}$  if  $P(t)$  goes from above to below  $p_-$  at time  $t_{\text{start}}$ . The ending time  $t_{\text{end}}$  of the event is defined as the first later instant at which  $P(t)$  takes values greater than  $p_-$ . The duration of the event is, thus,  $d = t_{\text{end}} - t_{\text{start}}$ . Figure 1 shows a sketch of a low-pressure event for  $p_- = -3.2$ .

If  $n(p_-, T)$  is the number of low-pressure events with threshold  $p_-$  detected from the histories of  $M$  particles evolving over a total time  $T$  in the turbulence field, the average rate (or frequency) of events with that threshold can be estimated as

$$\zeta(p_-) = \frac{n(p_-, T)}{MT}. \quad (23)$$

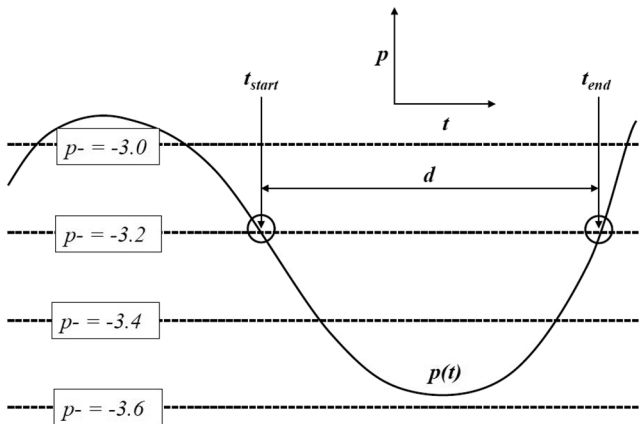


FIG. 1. Definition of a low-pressure event.

### III. RESULTS AND DISCUSSION

A total of  $M = 64^3$  nuclei are initially placed uniformly in a cubic setup in the turbulent velocity field. The initial distance between neighboring nuclei is four times the DNS grid spacing. The velocity field transports all the nuclei within the three-dimensional periodic domain of size  $2\pi \times 2\pi \times 2\pi$ . As discussed in Sec. II C, one in every four of the 90 000 DNS solutions available was used, i.e., 22 500 time steps were used for tracking of the nuclei. The corresponding nondimensional time is  $t = 97.065$  ( $\approx 380 t_\eta$  or  $25T_L$ ) with a time step size of  $4.3 \times 10^{-3}$  or  $t_\eta/60$ . Nuclei trajectories along with the corresponding pressure are recorded at all time steps for a set of cases with different nuclei sizes  $R_0$  and buoyancy parameters  $w$ . Table I shows the list of cases run for this study. The dependence on  $R_0$  is studied in the range of 0–0.05, but  $R_0$  up to 0.3 is used in Sec. IV to study cavitation inception. Note that the model equation (14) is rigorously valid up to  $R_0 \approx 0.08$ , which corresponds to twice the Kolmogorov length scale ( $\eta = 0.041$ ). At this size, the gas nuclei will interfere with the dissipation processes, occurring at the smallest scales. However, experimental evidence<sup>26</sup> shows that the overall turbulent kinetic energy dissipation rate is little affected at void fractions below 1%, a value at least two orders of magnitude higher than those of interest in this paper, justifying the one-way coupled approach used here. Low pressure structures are considerably larger than the largest nuclei sizes considered, so forces due to the pressure gradients are properly evaluated. Larger nuclei sizes will make inertial time to deviate from Eq. (11), but the trends are still valid, noting that for nuclei size of interest in this work, the drag coefficient differences with the Stokes drag law are limited to about 10% (see, for instance, Ref. 27). For gas nuclei in water,  $R_0$  will rarely exceed 0.05, and larger values are of interest to observe trends. Note in Eq. (10) that  $R_0$  is non-dimensionalized with  $\lambda$ . There may be situations where nuclei may be too small compared to  $\lambda$  and therefore behave as tracers, which would be the case of large scale turbulence compared to typical nuclei sizes ( $R_0 < 100 \mu\text{m}$ ). In these cases,  $Re_\lambda$  will also be typically large. On the other end, strong small scale turbulence will have small  $\lambda$ , and  $R_0$  can be large.

#### A. Basic statistics of pressure fluctuations

Pressure experienced by nuclei in homogeneous isotropic turbulence varies significantly depending on the size of the nuclei and

**TABLE I.** Nuclei sizes  $R_0$  and buoyancy parameters  $w$  considered for this study.<sup>a</sup> First row indicates the nuclei sizes, and the first column indicates buoyancy parameters. Checkmark (✓) indicates cases considered.

	0.00	0.01	0.02	0.03	0.04	0.05
0.0	✓	✓	✓	✓	✓	✓
1.0	✗	✓	✗	✓	✗	✓
2.0	✗	✓	✓	✓	✓	✓
4.0	✗	✓	✓	✓	✓	✓
6.0	✗	✗	✗	✗	✗	✓
8.0	✗	✓	✓	✓	✓	✓

<sup>a</sup>Some additional sizes larger than 0.05 have also been used for pressure statistics and cavitation inception computation. They will be mentioned when reported.

the magnitude of the buoyancy acting on them. The pressure gradient force increases with size due to the larger surface area, while Stokes drag increases linearly with radius, making larger nuclei more attracted toward the low-pressure regions. The larger nuclei experience lower average pressure, as shown in Fig. 2(a). The drop in average pressure decreases with increasing buoyancy. Higher buoyancy gives rise to a vertical drift of the nuclei, which counteracts the motion toward vortex cores caused by the pressure gradient. The fitting results of average pressure as a function of the radius  $R_0$  of the nuclei and of the buoyancy parameter  $w$  result in the approximation,

$$p_{\text{mean}} = -(75R_0^2 + 2R_0)e^{-w/2}, \quad (24)$$

shown as dashed lines in Fig. 2(a).

The variance  $\sigma_p^2$  of the pressure fluctuations, on the other hand, increases with increasing nuclei size and decreases with increasing buoyancy, as shown in Fig. 2(b). The combined dependence can be fitted as

$$\sigma_p^2 = (150R_0^2 + 3.75R_0)e^{-w/2} + 0.725 \quad (25)$$

(shown as dashed lines in this figure). The temporal derivative of the pressure fluctuations is very sensitive to buoyancy but much less to size. An appropriate fit, depicted with a dashed line in Fig. 2(c), reads

$$\sigma_{dp/dt}^2 = 1.1w^2 + 0.335w + 1.25. \quad (26)$$

The Lagrangian Taylor time scale  $\tau_p$ , defined as

$$\tau_p = \left[ \frac{\sigma_p^2}{\sigma_{dp/dt}^2} \right]^{1/2}, \quad (27)$$

shows a decay with increasing buoyancy. It increases slightly with the nuclei size ( $R_0$ ), especially if buoyancy is low [Fig. 2(d)]. Equa-

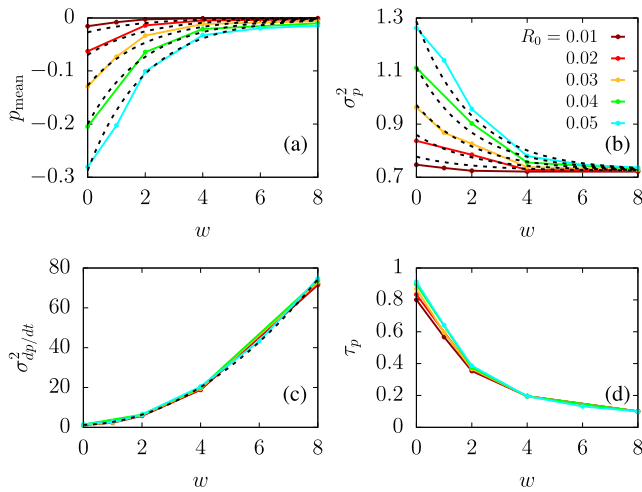


**FIG. 2.** Average pressure statistics of gas nuclei in homogeneous isotropic turbulence as functions of nuclei size and buoyancy. (a) Mean pressure fluctuation, (b) variance of pressure fluctuation, (c) variance of time-derivative of pressure fluctuation, and (d) Taylor timescale. Dashed lines in (a)–(c) correspond to (24)–(26), respectively.

tions (24)–(27) can be used to estimate pressure statistics, for instance, for cavitation inception models.

The behavior of these quantities when  $w = 0$  is consistent with the known higher attraction of larger nuclei toward the thin, very low-pressure vortex cores. Because the vortices have finite lifetime, this attraction to the vortex cores makes the nuclei to experience not only lower average pressures but also larger pressure variations. Buoyancy ( $w > 0$ ) counteracts this effect, which is reasonable since it adds a force that, in general, does not point toward the vortex core. Buoyancy also makes that the nuclei see, on average, the turbulent flow “passing by” at speed  $-w$ . This explains the quadratic increase  $\sigma_{dp/dt}^2 \sim w^2$  for larger  $w$ .

## B. Probability density function of pressure

Further insight into the interaction of finite-sized nuclei with vortex cores can be attained by studying the pressures experienced by the nuclei transported along Lagrangian trajectories. Figure 3(a) shows the pdf's of the pressure experienced by the nuclei for  $R_0$  varying from zero to 0.30.

Compared to the Eulerian pressure pdf, which coincides with that of  $R_0 = w = 0$ , the effect of nuclei size is to skew the distribution more and more toward negative pressures, as expected, up to  $R_0 \approx 0.1$ . The negative tail of the pdf keeps its exponential shape, with its logarithmic slope decreasing with nuclei size. For larger  $R_0$ , this trend seems to level off. We believe that two factors contribute to this saturation in the effect of  $R_0$ . First, the low-pressure vortices have a relatively small volume so that their inward pull can only attract a finite number of nuclei from their immediate neighborhood before they dissipate. In addition, larger nuclei have larger response times to the vortex attraction and arrive later to the low-pressure cores. For the larger sizes, the delay may become comparable to the lifetime of the vortices.

Figures 3(b) and 3(c) show the pdfs for various  $R_0$  at two other buoyancy values, namely,  $w = 4$  and 8. They confirm that buoyancy counteracts the attraction of nuclei toward low-pressure regions. The case with  $w = 4$  is particularly interesting. At this level of buoyancy, the pdf is independent of  $R_0$  for positive and mildly negative values of  $p$ , while a strong effect of size remains for lower pressures. This indicates that, as buoyancy is increased, it first destroys the correlation between positive and moderately negative pressure fluctuations and nuclei positions. The very low pressure fluctuations, associated with strong vortices, maintain their efficiency in trapping nuclei up to higher values of buoyancy. Eventually, as seen in the case  $w = 8$ , the whole pressure pdf coincides with the Eulerian one. To better illustrate this observation, in Fig. 4, we compare the pdfs obtained for different values of  $w$  in cases with  $R_0 = 0.05$ . The value  $w = 2$  already makes the pdf to coincide with the Eulerian one for  $p > -2$ . Increasing the value to  $w = 4$  extends the coincidence down to  $p > -5$ . It is remarkable that the probability of a nucleus being exposed to very low pressure ( $p < -12$ ) is practically unaffected by buoyancy unless  $w > 4$  (terminal velocity four times larger than the turbulence intensity  $u'$ ).

## C. Low-pressure events

From the pressure pdf, it is evident that the probability of a nucleus experiencing a fluid pressure below some given threshold

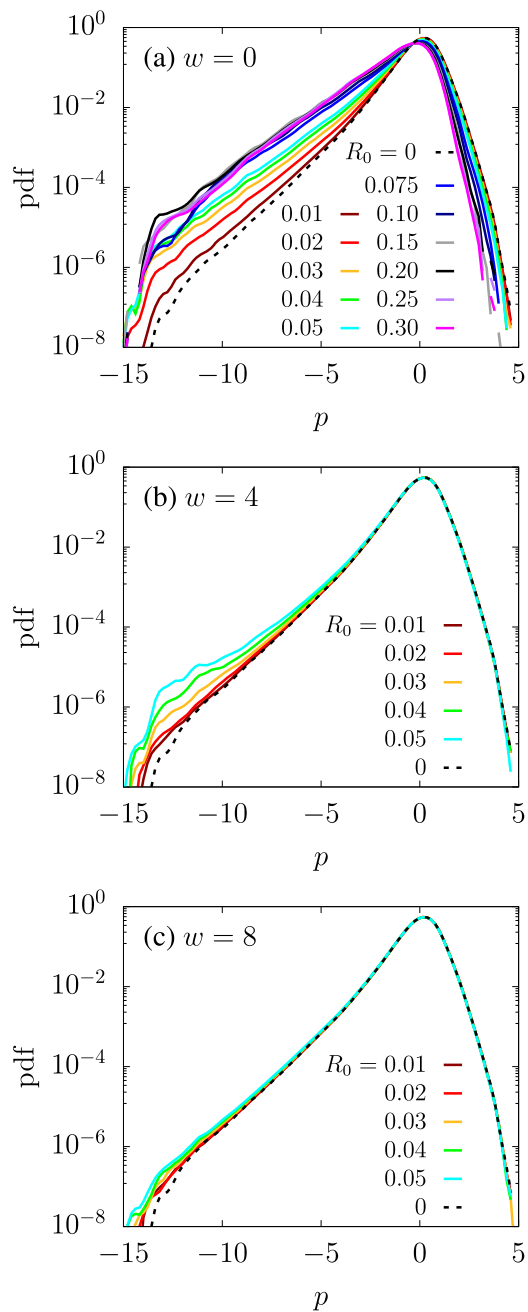


**FIG. 3.** Probability density functions of pressure fluctuations with different nuclei size for (a)  $w = 0$ , (b)  $w = 4$ , and (c)  $w = 8$ .

$p_-$  increases with its size and decreases with its terminal velocity. The fraction of time a nucleus spends at pressures below  $p_-$  can be computed as the cumulative distribution function (cdf), defined as

$$\text{cdf}(p_-) = \int_{-\infty}^{p_-} \text{pdf}(p) dp. \quad (28)$$

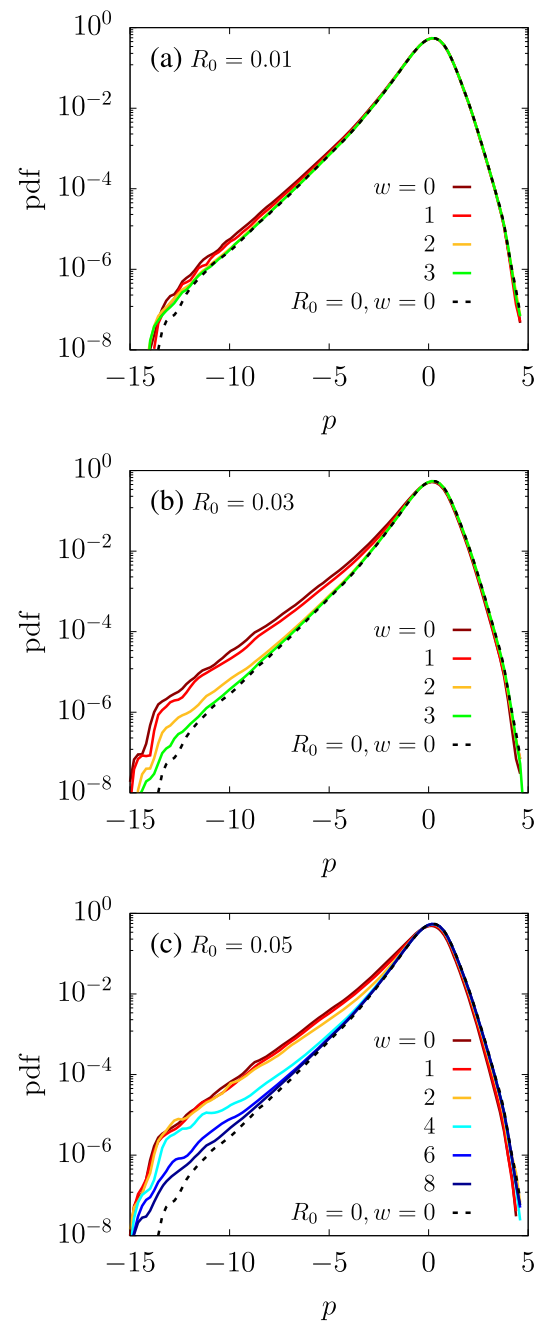


**FIG. 4.** Probability density functions of pressure fluctuations at different buoyancy conditions for (a)  $R_0 = 0.01$ , (b)  $R_0 = 0.03$ , and (c)  $R_0 = 0.05$ .

The pdf, on the other hand, does not say whether the nucleus undergoes many excursions below  $p_-$ , each lasting a very short time, or just a few long excursions. In fact,  $\text{cdf}(p_-)$  can be factored as the product of the average duration  $\bar{d}(p_-)$  and the average frequency  $\zeta(p_-)$  of events of threshold  $p_-$ . The effects of size and buoyancy on each of the factors are explored below.

**Figure 5** shows the average frequency of low-pressure events as a function of  $p_-$  for a range of nuclei sizes at  $w = 0, 4$ , and  $8$ . The plots corresponding to  $w = 0$  indicate that the attraction of larger nuclei toward vortex cores significantly increases the frequency of

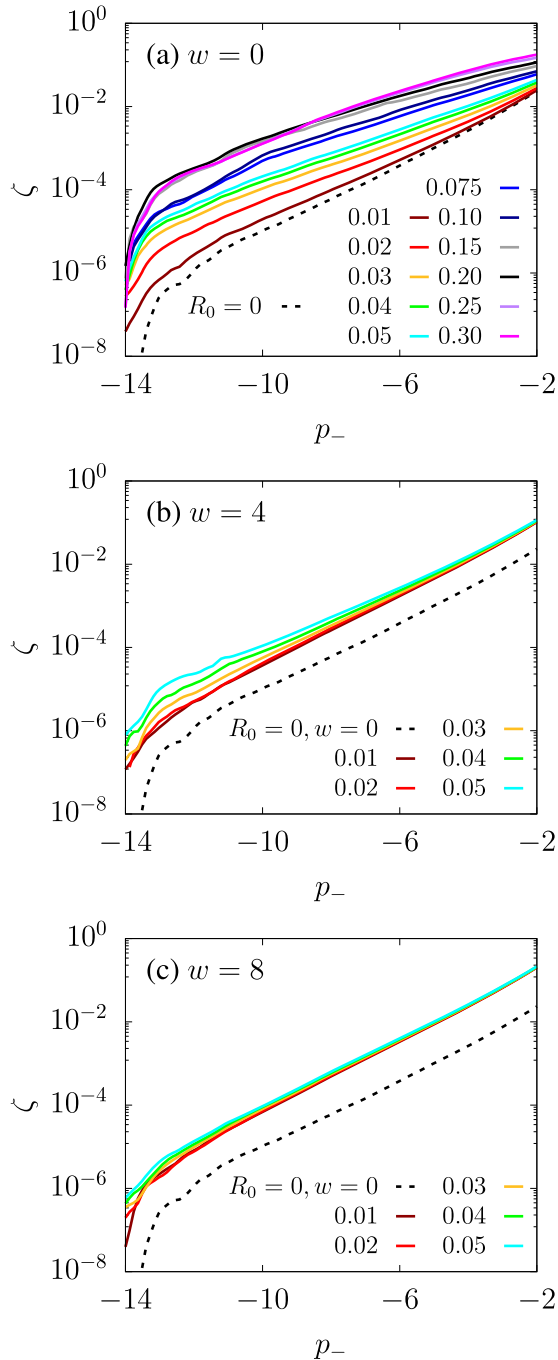


**FIG. 5.** Frequency of low-pressure fluctuation events with different nuclei sizes at buoyancy values (a)  $w = 0$ , (b)  $w = 4$ , and (c)  $w = 8$ .

low-pressure excursions. The average frequency increases by a factor of up to 300. This is more prominent for events with lower  $p_-$ , as is the saturation of the curves for  $R_0 \geq 0.15$ . **Figure 6** displays the average duration as a function of size. One can see that the changes in  $\bar{d}$  are much smaller than those in  $\zeta$ , and not monotonous. The duration increases with size for the smallest nuclei, as expected. However, for larger sizes, the trend is the opposite, which we attribute to the larger response time of larger nuclei making them to arrive later to the low-pressure region. Overall, in the absence of buoyancy, the dominant effect of size is that more nuclei enter the low-pressure vortical regions, and thus, the Lagrangian low-pressure events happen significantly more often.

The effect of buoyancy is apparent from Figs. 5(b) and 5(c). For very small nuclei ( $R_0 = 0.01$ ), which are not significantly trapped by vortices, increasing  $w$  produces an overall shift upward of the frequency curves. This is consistent with the increase in  $\sigma_{dp/dt}^2$  already discussed and is essentially a consequence of the average relative velocity between the fluid and the cloud of nuclei. For larger sizes, buoyancy has the additional effect of pulling the nuclei out of the vortex cores. As a result, practically no increase in  $\zeta$  with  $R_0$  is observed if  $w = 8$ , while at  $w = 4$ , a weak effect is visible and only

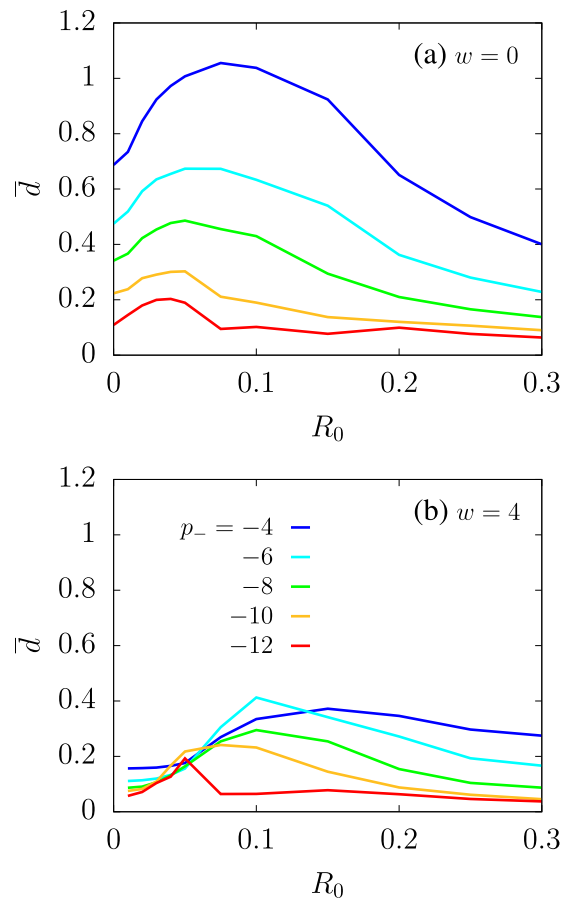


**FIG. 6.** Average duration of low-pressure fluctuation events with different nuclei sizes at buoyancy values (a)  $w = 0$  and (b)  $w = 4$ .

at very low values of  $p_-$ . These combined effects are clear when the effect of buoyancy is put forward by replotted the same data as in Fig. 7. For very small nuclei, the average frequencies at all pressure thresholds increase with  $w$  by the same factor, consistent

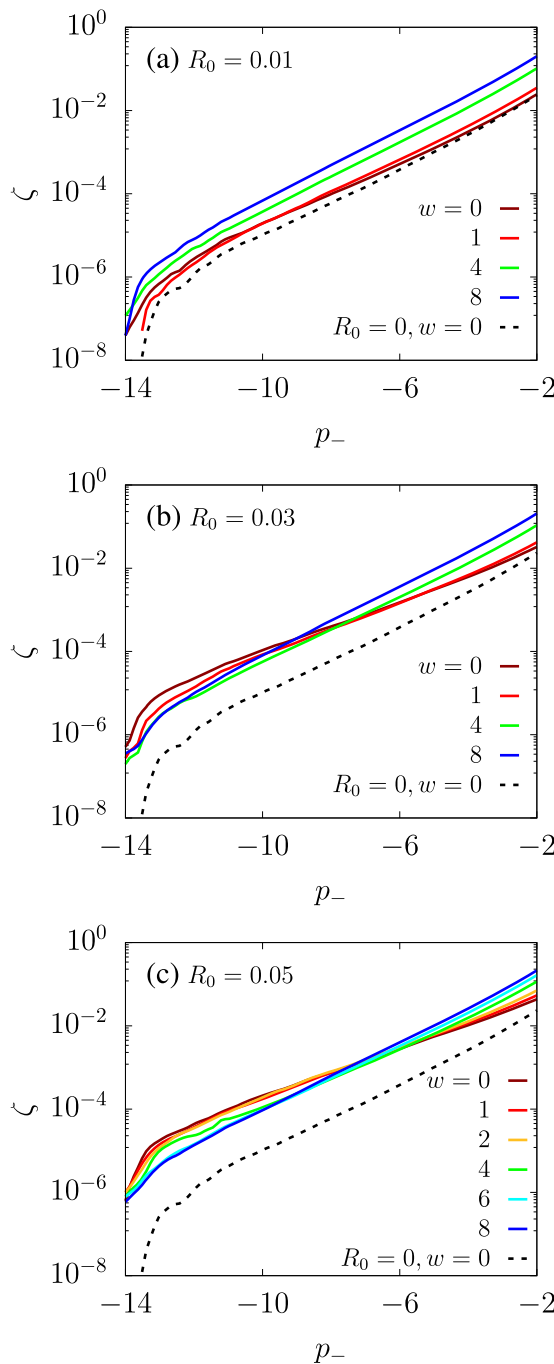


**FIG. 7.** Frequency of low-pressure fluctuation events at different buoyancy values for (a)  $R_0 = 0.01$ , (b)  $R_0 = 0.03$ , and (c)  $R_0 = 0.05$ .

with Lagrangian pressure pdf being independent of buoyancy and equivalent to the Eulerian one, as discussed in reference to Fig. 4(a). For larger nuclei, buoyancy disrupts their attachment to all but the strongest vortices so that the net effect [see Figs. 7(b) and 7(c)] is increasing the frequency of events for higher thresholds ( $p_- \approx -2$ ) and decreasing if for lower thresholds ( $p_- \approx -12$ ). The average duration of events at  $w = 4$  confirms this picture: in Fig. 6(a), there is an overall decrease in duration as compared to the  $w = 0$  case, especially for the smaller nuclei and higher values of  $p_-$ , while in Fig. 6(b), the average duration of events for the largest nuclei considered ( $R_0 = 0.3$ ) and the lowest thresholds ( $p_- = -10$  or  $-12$ ) are similar with and without buoyancy.

#### D. Concentration of nuclei

By careful observation of the distribution of nuclei at a given instant, one can notice their preferential concentration accompanying the vortex cores. An example is shown in Fig. 8, which is a snapshot of the nuclei colored with pressure. The blue filaments correspond to vortex cores, and they appear very well defined because of the increased density of nuclei there. Computational cells with two or more nuclei are shown in Fig. 9, again colored with pressure. These cells are quite rare, since the average density is  $64^3/256^3 = 0.016$  nuclei/cell. Their correlation with the low-pressure filaments in Fig. 8 is evident. For an average high concentration of nuclei in water of  $10^7$  nuclei/m<sup>3</sup> and a nuclei size of  $30 \mu\text{m}$ , 2 nuclei/cell correspond to a void fraction of 0.015%, low enough to still assume that nuclei are dilute.

Finally, the same visualization used in Fig. 8 is adopted in Fig. 10 to depict the effects of both size and buoyancy on the tendency of nuclei toward vortex cores. All snapshots correspond to the same instant and viewpoint of Fig. 8. Figure 10(a) shows the results corresponding to  $R_0 = 0.03$  and  $R_0 = 0.02$  at  $w = 0$ . As the nuclei size decreases, the filaments get blurred because fewer nuclei get to the vortex core. A similar blurring occurs in Fig. 10(b) as a result of increasing  $w$  to 2 and then 4, while keeping  $R_0 = 0.05$ ; notice, in Fig. 8, the stronger concentration of particles in cores for  $w = 0$ .

The contrast between Figs. 8 and 10 for concentration of bubbles in low pressure cores as the terminal velocity increases or nuclei

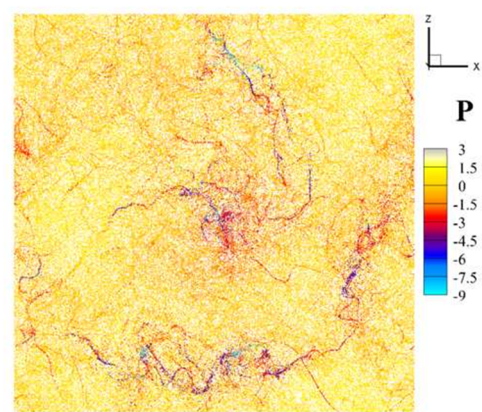


**FIG. 8.** Instantaneous lateral view of the fluid domain for the case with  $R_0 = 0.05$  and no buoyancy ( $w = 0$ ). Nuclei are shown as spheres colored with pressure.

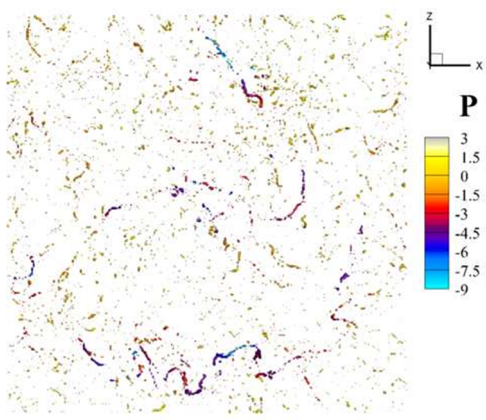


**FIG. 9.** Iso-surface of nuclei density at  $2 \text{ nuclei}/\text{dx}^3$  colored with pressure. Nuclei are of size  $R_0 = 0.05$ , and no buoyancy is acting. Filaments of nuclei subject to low pressure are clearly visible, showing that neighboring nuclei align themselves within the vortex cores and follow the core until it dissipates. When the core vorticity decays, the filament starts to diffuse and eventually disappears.

radius decreases is consistent with the quantitative results shown in Figs. 3 and 4. From the inspection of Fig. 3, the conditions in Fig. 10(a) still produce lower pressures than tracer particles ( $R_0 = 0$ ), which are essentially randomly distributed in the flow.

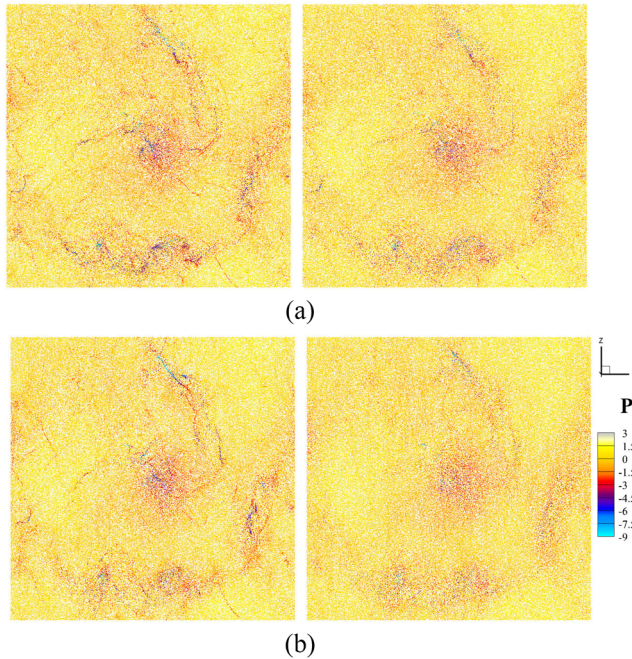


**FIG. 10.** Snapshots of a lateral view of the nuclei in the turbulent field colored with pressure. (a) Cases with  $w = 0$  and  $R_0 = 0.03$  (left) and  $R_0 = 0.02$  (right). (b) Cases with  $R_0 = 0.05$  and  $w = 2$  (left) and  $w = 4$  (right).

#### IV. APPLICATION TO CAVITATION INCEPTION

The low-pressure fluctuations studied above, under suitable conditions, can produce the cavitation of a gaseous particle even if the average pressure is above vapor pressure. This phenomenon is studied here by solving the Rayleigh-Plesset equation<sup>1</sup> for each nucleus as it is subjected to the pressure along its tracked trajectory. This model is valid for small and very disperse gaseous particles and thus is especially well-suited for incipient cavitation conditions. The Rayleigh-Plesset equation describes the evolution of the bubble radius  $R(t)$  (hereafter, the notation without tilde represents dimensional variables) that results from a time-dependent local pressure  $P(t)$ . It reads

$$\rho_\ell \left( \frac{3}{2} \dot{R}^2 + R \ddot{R} \right) + \frac{4\mu_\ell \dot{R}}{R} = p_{\text{vap}} + \underbrace{\left( p_{\text{eq}} + \frac{2S}{R_{\text{eq}}} - p_{\text{vap}} \right) \frac{R_{\text{eq}}^{3\gamma}}{R^{3\gamma}} - \frac{2S}{R}}_{F_{\text{NN}}(R)} - P(t), \quad (29)$$

where  $\dot{R} = dR/dt$ ,  $\ddot{R} = d^2R/dt^2$ ,  $\rho_\ell$  and  $\mu_\ell$  correspond to the fluid density and viscosity, respectively,  $p_{\text{vap}}$  is the vapor pressure of the liquid (temperature dependence is neglected),  $S$  is the surface tension,  $\gamma$  is the polytropic exponent of the non-condensable gas, and  $R_{\text{eq}}$  corresponds to the radius that the bubble adopts, when neglecting gravitational effects is in equilibrium with the liquid at rest at a uniform temperature  $T_{\text{eq}}$  and external pressure  $p_{\text{eq}}$ .

Equation (29) is an ordinary differential equation that is driven by its right-hand side,  $F_{\text{NN}}(R) - P(t)$ . The function  $F_{\text{NN}}(R)$  is depicted in Fig. 11 for some typical values of the parameters. Its minimum value, which takes place at a radius that we denote by  $R_*$ , is known as *cavitation pressure* or *Blake threshold pressure*,<sup>28</sup>

$$P_{\text{cav}} = \min_{R>0} F_{\text{NN}}(R) = F_{\text{NN}}(R_*) = p_{\text{vap}} - \frac{3\gamma-1}{3\gamma} \left( \frac{(2S)^{3\gamma}}{3\gamma(p_{\text{eq}} + \frac{2S}{R_{\text{eq}}} - p_{\text{vap}})R_{\text{eq}}^{3\gamma}} \right)^{\frac{1}{3\gamma-1}}. \quad (30)$$

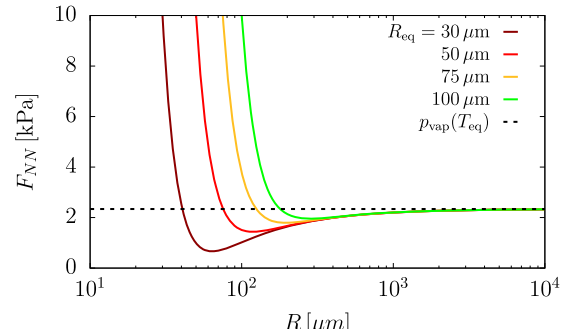


**FIG. 11.** Function  $F_{\text{NN}}(R)$  for the typical values of the parameters and  $R_{\text{eq}}$  equal to  $30 \mu\text{m}$ ,  $50 \mu\text{m}$ ,  $75 \mu\text{m}$ , and  $100 \mu\text{m}$ . Specifically:  $T_{\text{eq}} = 300 \text{ K}$ ,  $p_{\text{vap}}(T_{\text{eq}}) = 2340 \text{ Pa}$ ,  $p_{\text{eq}} = 10 \text{ kPa}$ ,  $S = 7 \times 10^{-2} \text{ Pa m}$ , and  $\gamma = 1.4$ .

If  $P(t)$  is a given constant  $P_0$ , and if  $P_0 > p_{\text{cav}}$ , the bubble radius stabilizes at a value  $R_0 < R_*$ , which satisfies  $F_{NN}(R_0) = P_0$ . If  $P_0 < p_{\text{vap}}$ , two solutions exist for  $R_0$ , but the larger one ( $>R_*$ ) is mechanically unstable. On the other hand, if  $P_0 < p_{\text{cav}}$ , the initially tiny bubble grows rapidly and reaches detectable sizes, i.e., a *cavitation event* takes place. For non-constant functions  $P(t)$  that dip below  $p_{\text{cav}}$  for some limited time, it is not obvious whether the bubble will grow to detectable sizes or not.

In this section, we investigate the solutions of (29) with  $P(t) = P_0 + P_1(t)$ , where  $P_0 > p_{\text{cav}}$  and  $P_1(t)$ , which has zero mean, corresponds to the pressure fluctuations along the trajectories described in Secs. II and III. That is, the *dimensional* pressure history of the  $i$ th simulated particle is taken as

$$P^{(i)}(t) = P_0 + \rho_\ell u'^2 \tilde{P}^{(i)} \left( \frac{u'}{\lambda} t \right), \quad (31)$$

where  $\tilde{P}^{(i)}$  is a non-dimensional pressure history computed as described in Sec. II and discussed in Sec. III. The corresponding solution models the evolution  $R^{(i)}(t)$  of the particle's radius. We vary the pressure  $P_0$  and simulate bubbles of different sizes. The size is specified as the radius  $R_0$  that is in equilibrium at pressure  $P_0$  [i.e., in (29), we impose  $p_{\text{eq}} = P_0$  and  $R_{\text{eq}} = R_0$ ]. The initial conditions to start the integration are  $\dot{R}(0) = 0$  and  $R(0)$  such that  $F_{NN}(R(0)) = P(0)$ . Note that  $P(0)$ , which varies from bubble to bubble, is, in general, different from the average pressure  $P_0$  of the flow.

The material parameters were given fixed values:  $\rho_\ell = 1000 \text{ kg/m}^3$ ,  $\mu_\ell = 10^{-3} \text{ Pa s}$ ,  $S = 0.07 \text{ Pa m}$ ,  $\gamma = 1.4$ , and  $p_{\text{vap}} = 2340 \text{ Pa}$ . These values are representative of water under ambient conditions. The numerical procedure adopted is a fourth-order embedded Runge–Kutta method with an adaptive time step<sup>29</sup> applied to a scaled version of the equation (to reduce round-off errors).

The main criterion adopted here to define a cavitation event is that the bubble radius reaches the value  $10R_0$ . As discussed by Hilgenfeldt *et al.*,<sup>28</sup> this criterion ensures that the bubble will experience a strong collapse when pressure goes back above  $p_{\text{cav}}$ , which can be detected by acoustic methods. Another criterion used for comparison corresponds to visual detection. It considers that the bubble cavitates when it reaches some fixed size that can be visually detected (we adopted  $R = 250 \mu\text{m}$ ), regardless of the initial size.

If bubble  $i$  satisfies the cavitation criterion at time  $t_*$ , then the integration of (29) is stopped, the cavitation event is counted and another bubble is reseeded at a later time  $t_{**}$  such that  $P^{(i)}(t_{**}) > p_{\text{cav}}$ , with radius  $R^{(i)}(t_{**})$  such that  $F_{NN}(R^{(i)}(t_{**})) = P^{(i)}(t_{**})$ .

By changing the values of  $P_0$ ,  $R_0$ , and  $u'$ , different cases were considered in the investigation of cavitation rates. For a given bubble size and turbulence intensity,  $P_0$  are the given values that start at 3 kPa with increments of 200 Pa until no cavitation is observed. The values of  $R_0$  are obtained from the values of  $\tilde{R}_0$  whose trajectories were previously calculated. They are also constrained by the choice of  $u'$ , since  $R_0 = \tilde{R}_0 \lambda$ ,  $\lambda = Re_\lambda v/u'$ , and  $Re_\lambda$  is fixed at 150. We simulated the cases of  $u' = 0.75 \text{ m/s}$  and  $1 \text{ m/s}$ , and the corresponding values of  $R_0$  are presented in Table II. No buoyancy effect was considered ( $\tilde{w} = 0$ ) as the terminal velocities for these bubbles are several orders of magnitude smaller than  $u'$ .

Figure 12 shows two examples of time series of  $P(t)$  and their corresponding solutions of (29), obtained for  $R_0 = 30 \mu\text{m}$ ,  $P_0 = 3$

**TABLE II.** Bubble sizes considered in the cavitation simulation for  $Re_\lambda = 150$  and  $\tilde{w} = 0$ .

$\tilde{R}_0$	$u' = 0.75 \text{ m/s}$		$u' = 1 \text{ m/s}$	
	$\lambda = 2 \times 10^{-4} \text{ m}$	$R_0 (\mu\text{m})$	$\lambda = 1.5 \times 10^{-4} \text{ m}$	$R_0 (\mu\text{m})$
0.05		10		7.5
0.10		20		15.0
0.15		30		22.5
0.20		40		30.0
0.25		50		37.5
0.30		60		45.0

kPa, and  $u' = 1 \text{ m/s}$ . Note that the size of the bubble does not change significantly until  $P(t)$  takes values below  $p_{\text{cav}}$ . This justifies the use of the trajectory of a bubble with constant size. It also explains why in this section, the (dimensional) threshold to define a *low-pressure event* is  $p_- = p_{\text{cav}}$ . The bubble in Fig. 12(a) does not reach the cavitation criterion and eventually collapses. Note that the integration of (29) is also stopped when collapse occurs, since it is of no interest to our study and heavily burdens the computations. Also remarkable is the effect of inertia in causing a significant delay (of more than one Taylor timescale) between the increase in pressure to values above  $p_{\text{cav}}$  and the collapse of the bubble [Fig. 12(a)]. Figure 12(b), on the other hand, shows  $R(t)$  for a bubble that ends up cavitating. The pressure fluctuation in this case goes further below  $p_{\text{cav}}$  and for a longer time.

The average rate of low-pressure events  $f_{\text{lp}}$  and the average cavitation rate  $f_{\text{cav}}$  were estimated as

$$f_{\text{lp, cav}} = \frac{N_{\text{lp, cav}}}{M(\lambda T/u')}, \quad (32)$$

where  $N_{\text{lp}}$  (or  $N_{\text{cav}}$ ) is the number of low-pressure (or cavitation) events counted in the simulation,  $M$  is the total number of particles

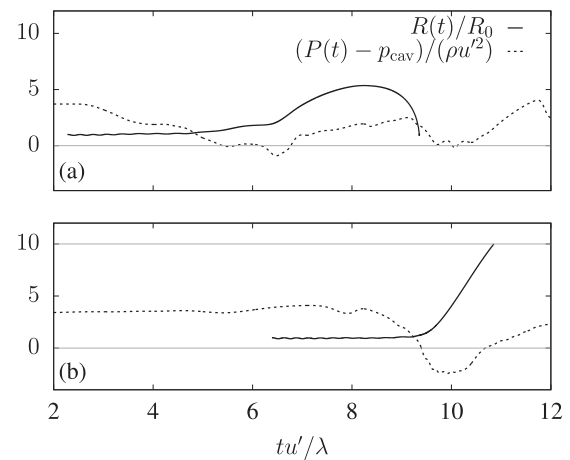


**FIG. 12.** Examples of pressure histories (dashed lines) and corresponding evolution of bubble radius (solid lines) for  $R_0 = 30 \mu\text{m}$  and  $u' = 1 \text{ m/s}$ . Both bubbles experience  $P(t) < p_{\text{cav}}$ , while the one in (a) does not reach cavitation criterion, the one in (b) reaches the  $R(t) = 10R_0$  criterion and cavitates.

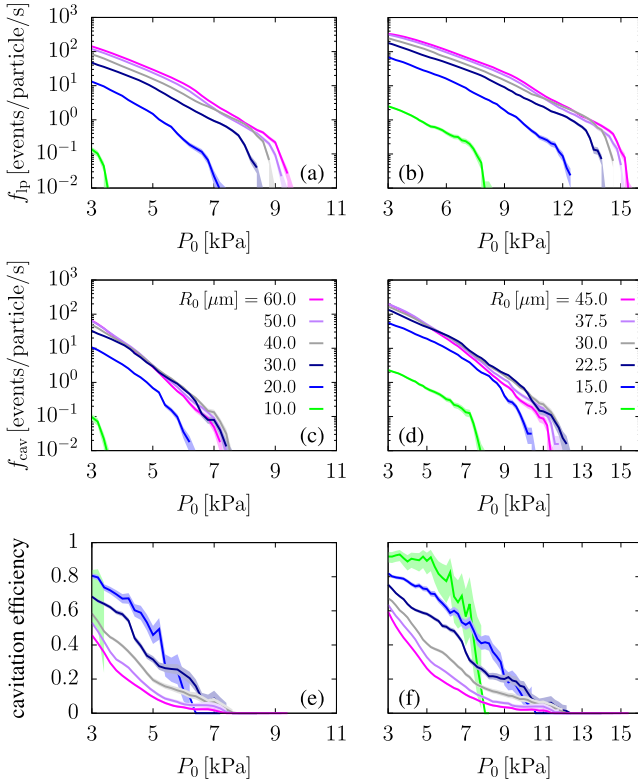
( $M = 32^3$  for all cases), and  $\tilde{T}$  is the non-dimensional DNS simulated time ( $\tilde{T} = 28.8$ ).

Figure 13 presents the estimated values of  $f_{lp}$  for each case tested, and it shows the expected increase with  $R_0$  and roughly exponential decrease with  $P_0$ . Also shown are plots of  $f_{cav}$  for which the dependence on  $R_0$  is less obvious. This is explained by the larger inertia of larger bubbles, which reduces the *cavitation efficiency* [defined as  $f_{cav}/f_{lp}$ , see Figs. 13(e) and 13(f)].

The most immediate use of  $f_{cav}$  estimations is the prediction of the average rate  $F$  of cavitation events (in events/m<sup>3</sup>/s) in some region of a flow in which homogeneous and isotropic turbulence conditions can be assumed with mean pressure  $P_0$  and turbulent variables  $u'$  and  $\lambda$ . If  $\phi(R)$  is the nuclei size distribution function (in particles/m<sup>4</sup>), then

$$F = \int_{R_{\min}}^{R_{\max}} \phi(R) f_{cav}(R) dR, \quad (33)$$

where  $R_{\min}$  and  $R_{\max}$  are the minimum and maximum radii of the particles in the distribution. Such  $F$  would decrease with increasing  $P_0$ , and cavitation inception can thus be defined as the highest value of  $P_0$  for which  $F$  is large enough to be detectable.



**FIG. 13.** Average rate of low-pressure events [ $f_{lp}$ , (a) and (b)], average rate of cavitation events [ $f_{cav}$ , (c) and (d)], and cavitation efficiency [ $f_{cav}/f_{lp}$ , (e) and (f)] for  $u' = 0.75$  m/s (left panels) and  $u' = 1$  m/s (right panels). Shaded area corresponds to one standard deviation in (a)–(d) (assuming a Poisson process) and a confidence interval of 95% in (e) and (f) (assuming a binomial process with the fixed number of events).

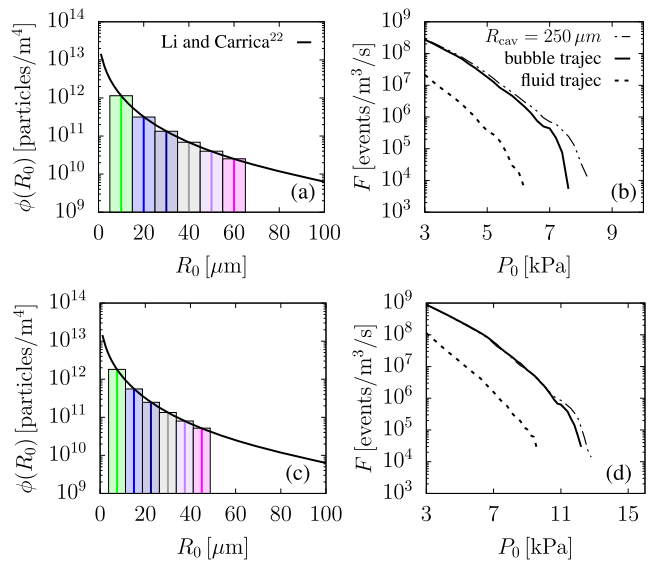


**FIG. 14.** Density distribution of nuclei [ $\phi(R_0)$ , (a) and (c)] from Li and Carrica<sup>30</sup> and average cavitation rate [ $F$ , (b) and (d)] for  $u' = 0.75$  m/s (upper panels) and  $u' = 1$  m/s (lower panels). Rectangles in (a) and (c) correspond to the area used in the numerical integration of (33). In (b) and (d), solid lines use bubble trajectories in the calculation, and dashed line uses fluid trajectories (or  $\tilde{R}_0 = 0$ ). The solid line uses the cavitation criterion of  $10R_0$ , and the dotted dashed line corresponds to the cavitation criterion of  $250 \mu\text{m}$ .

Figure 14 shows an estimation of  $\phi(R)$  obtained by fitting several experimental nuclei size distribution functions, with a nuclei void fraction of  $9 \times 10^{-7}$  considering nuclei up to  $100 \mu\text{m}$ .<sup>30</sup> To use the average cavitation rates computed above, we approximate  $F$  numerically by

$$F \approx \sum_{i=1}^6 \phi(R_{0i}) f_{cav}(R_{0i}) W_i, \quad (34)$$

where  $i$  runs over the six available values of  $R_0$ , with the weights  $W_i$  depicted by the columns superimposed to the curve  $\phi(R)$ . This approximates the main part of the integral, since at the lower end of the integral, the cavitation rate  $f_{cav}$  is already approaching zero [see Figs. 13(c) and 13(d)], and on the other end of the integral, the value of the density distribution decreases exponentially. The numerical values of  $F$  are shown on the right column of Fig. 14. Assuming a detectability threshold of  $10^5$  events/m<sup>3</sup>/s, the effect of turbulent fluctuations is that inception is predicted at  $P_0 = 7.5$  kPa when  $u' = 0.75$  m/s and at  $P_0 = 12$  kPa when  $u' = 1$  m/s. This estimation does not change significantly if the cavitation criterion is that  $R(t)$  reaches  $250 \mu\text{m}$ , instead of  $10R_0$  [see Figs. 14(b) and 14(d)]. However, these values would be underestimated (5.5 kPa and 9 kPa, respectively) if the cavitation computations were performed with the pressure histories along *fluid* trajectories (equivalent to  $R_0 = 0$ ).

## V. SUMMARY AND CONCLUSION

The Lagrangian pressure statistics of gas nuclei in homogeneous isotropic turbulence at  $Re_\lambda = 150$  have been studied and

reported in this article. A DNS HIT database has been created and stored at Universidad Politécnica de Madrid, Spain, with very fine temporal resolution to ensure accurate tracking of gas nuclei in the turbulent flow field and long simulation time ( $\approx 380t_\eta$ ) to provide statistically significant results. A large number of non-interacting point particles were seeded in the turbulence velocity field and transported according to the Maxey–Riley equation. The trajectories and pressure histories were recorded, and the statistics of low-pressure events were determined. It was possible to visualize the association of turbulent structures with preferential concentration of the nuclei and to study the dependence of the variables of interest on the size of the nuclei and on their buoyancy-induced terminal velocity. Note that the simulations are one-way coupled in that the forces exerted by the particles on the fluid are neglected. It should also be mentioned that the model did not include the effects of Faxen correction and Basset history forces. This study covered a wide range of sizes, corresponding to the Stokes number ( $\tau/t_\eta$  in our notation) from 0 to 1.

Strong vortices attract larger nuclei toward their low-pressure cores as stronger pressure gradients there increase the relative velocity pointing toward the center of the vortical filaments. When the size of the nuclei is larger, more nuclei concentrate around the vortex cores. As a result, the mean pressure on the nuclei decreases and the pressure variability becomes larger as nuclei more often probe the very low pressures of vortex cores. The pdf of pressure responds very significantly to any change in size of the nuclei. As the size is increased, the super-exponential tail of the pdf (toward negative pressures) moves up as the probability of nuclei being in the low-pressure regions increases. On the positive-pressure side of the pdf, the trend is downward, which indicates that lesser nuclei are present in the higher pressure regions. The average frequency of low-pressure events behaves accordingly, increasing with size by a factor of up to 300 as  $R_0$  goes from 0 to 0.15 and then leveling off. The average duration of low-pressure events, on the other hand, varies much less with size and in a non-monotonous way.

Gravity acts on bubbles as a buoyant force that can be characterized by the vertical terminal velocity  $w$  in a still fluid. We considered cases with no buoyancy ( $w = 0$ ) and others with moderate ( $w \approx u'$ ) to very high buoyancy ( $w = 8u'$ ). Buoyancy has interesting consequences on the pressure statistics of the nuclei. As a gravitational pressure gradient, it competes with the flow-induced pressure gradient that attracts nuclei toward the vortex cores so that as buoyancy is increased only the strongest vortices (and eventually not even them) can capture nuclei. The effect on the pressure pdf of finite-sized bubbles is to make it tend to the  $R_0 = 0$  (Eulerian) pdf as buoyancy is increased; this tendency is slower at the lowest pressure values. The effect on the frequency of low-pressure fluctuations is similar but superimposed to an overall shift upward produced by buoyancy. This shift results from the average relative velocity  $\approx w$  of the nuclei with respect to the fluid, which also induces a reduction in the average duration of low-pressure events.

The pressure fluctuations experienced by the nuclei can make them cavitate in homogeneous turbulence with average pressure  $P_0$  significantly above the vapor pressure. The cavitation frequency strongly depends on  $P_0$  and on the size of the nuclei. The latter affects not only the trajectories and thus the pressure history undergone by the nuclei but also the efficiency with which low-pressure fluctuations make the nuclei to cavitate. Calculations were

performed to quantify these phenomena, and the results were then applied to predict the value of  $P_0$  that would correspond to incipient cavitation with a realistic polydisperse nuclei distribution. At a turbulent intensity  $u'$  of 0.75 m/s, inception is predicted at 7 kPa, while if  $u' = 1$  m/s, the prediction increases to 12 kPa. Such high values show that the fluctuations studied in this work can have technologically relevant consequences.

Due to the unavailability of very fine time-resolved DNS databases of turbulent flow at higher Reynolds number, this work has been limited to  $Re_\lambda = 150$ . In many situations of turbulent cavitating flow, the Reynolds number can be much larger. La Porta *et al.*<sup>31</sup> define the  $Re_\lambda$  using the velocity fluctuations and the Taylor microscale at the scale of their experiment, yielding  $Re_\lambda$  larger than 1600. We are motivated by estimating sub-grid scale pressure fluctuations in Computational Fluid Dynamics (CFD) simulations to improve the computation of cavitation inception.<sup>7</sup> For a CFD simulation with LES, the Taylor Reynolds number at the sub-grid level can be estimated from the residual turbulent kinetic energy and the dissipation as  $Re_\lambda \approx 1.5\epsilon^{\frac{1}{6}}\left(\frac{\Delta}{\pi}\right)^{\frac{2}{3}}\sqrt{\frac{15}{v}}$ . This in most cases yields for properly resolved LES  $Re_\lambda < 400$ , and more typically  $Re_\lambda \sim 100$ . Note that as the grid spacing  $\Delta$  decreases,  $Re_\lambda$  decreases, eventually resulting in a DNS computation where all pressure fluctuations are explicitly resolved and no pressure fluctuations at the sub-grid scale exist. Based on this analysis,  $Re_\lambda = 150$  is a reasonable parameter for studying sub-grid scale pressure fluctuations. An increase in  $Re_\lambda$  results in lower minimum pressures and extended low pressure tails in the pdf's, as described by Cao *et al.*<sup>12</sup> and Bappy *et al.*,<sup>13</sup> while lower  $Re_\lambda$  yield milder pressure fluctuations. Future work will focus on creating databases that characterize low-pressure fluctuations and cavitation at a range of higher and lower  $Re_\lambda$ .

## ACKNOWLEDGMENTS

This research was sponsored by the U.S. Office of Naval Research through MURI (Grant No. N00014-17-2676), University of Minnesota lead institution (Program Manager: Dr. Ki-Han Kim). M.H.B.'s visit to ETSIAE was funded, in part, by the Coturb program of the European Research Council. G.C.B. and L.S.F. acknowledge support from the São Paulo Research Foundation (FAPESP, Brazil) (Grant Nos. 2018/08752-5 and 2018/24284-1, respectively).

## DATA AVAILABILITY

The data that support the findings of this study are available from the corresponding author upon reasonable request.

## REFERENCES

- C. E. Brennen, *Cavitation and Bubble Dynamics* (Cambridge University Press, 2013).
- K. A. Mørch, "Cavitation inception from bubble nuclei," *Interface Focus* **5**, 20150006 (2015).
- R. E. Arndt and W. K. George, *Pressure Fields and Cavitation in Turbulent Shear Flows* (National Academy of Sciences, 1979), pp. 327–339.
- K. Agarwal, O. Ram, J. Wang, Y. Lu, and J. Katz, "Measuring the 3D pressure field and relating it to cavitation inception in a turbulent shear layer," in 33rd Symposium on Naval Hydrodynamics, 2020.

- <sup>5</sup>N. A. Chang, J. Choi, R. Yakushiji, and S. L. Ceccio, "Cavitation inception during the interaction of a pair of counter-rotating vortices," *Phys. Fluids* **24**, 014107 (2012).
- <sup>6</sup>M. Liu, L. Tan, and S. Cao, "Cavitation–vortex–turbulence interaction and one-dimensional model prediction of pressure for hydrofoil ALE15 by large eddy simulation," *J. Fluids Eng.* **141**, 021103 (2018).
- <sup>7</sup>M. Bappy, J. E. Martin, J. Li, G. C. Buscaglia, and P. M. Carrica, "A stochastic approach to cavitation inception prediction," in *Proceedings of the Sixth International Symposium on Marine Propulsors*, edited by M. Felli and C. Leotardi, 26–30 May 2019, Rome, Italy (National Research Council of Italy, Rome, Italy, 2019), Vol. 2, pp. 91–98.
- <sup>8</sup>G. K. Batchelor, "Pressure fluctuations in isotropic turbulence," *Math. Proc. Cambridge Philos. Soc.* **47**, 359–374 (1951).
- <sup>9</sup>M. S. Uberoi, *Correlations Involving Pressure Fluctuations in Homogeneous Turbulence* (National Aeronautics and Space Administration, 1954).
- <sup>10</sup>A. Pumir, "A numerical study of pressure fluctuations in three-dimensional, incompressible, homogeneous, isotropic turbulence," *Phys. Fluids* **6**, 2071–2083 (1994).
- <sup>11</sup>M. Holzer and E. D. Siggia, "Turbulent mixing of a passive scalar," *Phys. Fluids* **6**, 1820–1837 (1994).
- <sup>12</sup>N. Cao, S. Chen, and G. D. Doolen, "Statistics and structures of pressure in isotropic turbulence," *Phys. Fluids* **11**, 2235–2250 (1999).
- <sup>13</sup>M. Bappy, P. M. Carrica, and G. C. Buscaglia, "Lagrangian statistics of pressure fluctuation events in homogeneous isotropic turbulence," *Phys. Fluids* **31**, 085111 (2019).
- <sup>14</sup>S. Balachandar and J. K. Eaton, "Turbulent dispersed multiphase flow," *Annu. Rev. Fluid Mech.* **42**, 111–133 (2010).
- <sup>15</sup>T. O'hern, "An experimental investigation of turbulent shear flow cavitation," *J. Fluid Mech.* **215**, 365–391 (1990).
- <sup>16</sup>B. Gindroz and M. L. Billet, "Influence of the nuclei on the cavitation inception for different types of cavitation on ship propellers," *J. Fluids Eng.* **120**, 171–178 (1998).
- <sup>17</sup>Y.-C. Wang, "Effects of nuclei size distribution on the dynamics of a spherical cloud of cavitation bubbles," *J. Fluids Eng.* **121**, 881–886 (1999).
- <sup>18</sup>G. L. Chahine, "Nuclei effects on cavitation inception and noise," in 25th Symposium on Naval Hydrodynamic, 2004.
- <sup>19</sup>M. Khoo, J. Venning, B. Pearce, and P. Brandner, "Statistical aspects of tip vortex cavitation inception and desinence in a nuclei deplete flow," *Exp. Fluids* **61**, 145 (2020).
- <sup>20</sup>M. H. Bappy, A. Vela-Martin, G. C. Buscaglia, P. M. Carrica, and L. S. Freire, "Effect of bubble size on Lagrangian pressure statistics in homogeneous isotropic turbulence," *J. Phys.: Conf. Ser.* **1522**, 012002 (2020).
- <sup>21</sup>V. Mathai, D. Lohse, and C. Sun, "Bubbly and buoyant particle-laden turbulent flows," *Annu. Rev. Condens. Matter Phys.* **11**, 529–559 (2020).
- <sup>22</sup>G. R. Ruetsch and E. Meiburg, "On the motion of small spherical bubbles in two-dimensional vortical flows," *Phys. Fluids* **5**, 2326–2341 (1993).
- <sup>23</sup>M. R. Maxey and J. J. Riley, "Equation of motion for a small rigid sphere in a nonuniform flow," *Phys. Fluids* **26**, 883–889 (1983).
- <sup>24</sup>F. Toschi and E. Bodenschatz, "Lagrangian properties of particles in turbulence," *Annu. Rev. Fluid Mech.* **41**, 375–404 (2009).
- <sup>25</sup>T. R. Auton, J. C. R. Hunt, and M. Prud'Homme, "The force exerted on a body in inviscid unsteady non-uniform rotational flow," *J. Fluid Mech.* **197**, 241–257 (1988).
- <sup>26</sup>J. Lelouvetel, M. Nakagawa, Y. Sato, and K. Hishida, "Effect of bubbles on turbulent kinetic energy transport in downward flow measured by time-resolved PTV," *Exp. Fluids* **50**, 813–823 (2011).
- <sup>27</sup>M. Ishii and N. Zuber, "Drag coefficient and relative velocity in bubbly, droplet or particulate flows," *AICHE J.* **25**, 843–855 (1979).
- <sup>28</sup>S. Hilgenfeldt, M. P. Brenner, S. Grossmann, and D. Lohse, "Analysis of Rayleigh-Plesset dynamics for sonoluminescing bubbles," *J. Fluid Mech.* **365**, 171–204 (1998).
- <sup>29</sup>J. R. Dormand and P. J. Prince, "A family of embedded Runge–Kutta formulae," *J. Comput. Appl. Math.* **6**, 19–26 (1980).
- <sup>30</sup>J. Li and P. M. Carrica, "A polydisperse cavitation model," in 33rd Symposium on Naval Hydrodynamics, 2020.
- <sup>31</sup>A. La Porta, G. A. Voth, F. Moisy, and E. Bodenschatz, "Using cavitation to measure statistics of low-pressure events in large-Reynolds-number turbulence," *Phys. Fluids* **12**, 1485–1496 (2000).